# Improving hydrogen storage performance of Mg-based alloy through microstructure optimization

Jing Wen, Patricia de Rango, Nathalie Allain, Laetitia Laversenne, Thierry Grosdidier

# Improving hydrogen storage performance of Mg-based alloy through microstructure optimization

Jing Wen[a,b,*], Patricia de Rango[a,*], Nathalie Allain[b,c], Laetitia Laversenne[a], Thierry Grosdidier[b,c]

[a]Université Grenoble Alpes, CNRS, Institut Néel, 38000 Grenoble, France

[b]Laboratoire d'Excellence DAMAS, Université de Lorraine, CNRS, 57000 Metz, France

[c]Laboratoire d'Etude des Microstructures et de Mécanique des Matériaux (LEM3), Université de Lorraine, CNRS, Arts et Métiers ParisTech, 57000 Metz, France

## Abstract

Different fast forging processes are used for microstructure optimization in an attempt to improve hydrogen storage in Mg-based composites obtained from a mixture of Mg-22 wt.% Ni powders. First, fast forging is employed at room temperature to change the amount of structural defects, produce fine grains and modify crystallographic textures. The effects of such microstructure modifications (including the exact nature of phases) on the H-storage behavior are investigated. A Mg {0001} basal fiber texture develops upon fast cold forging, which facilitates the initial activation of hydrogenation while, owing to the high stability of the $MgH_2$ hydride, the kinetics of desorption remains rather slow. Second, to promote hydrogen desorption, forging is conducted at elevated temperature to form $Mg_2Ni$ phase. Interestingly, for this sample, faster desorption is recorded while slower absorption kinetics is obtained due to the occurrence of dynamic recrystallization inducing weaker texture and lower amount of structural defects. Third, annealing followed by cold forging is used to produce a microstructure consisting of fragmented $Mg_2Ni$ lamellae embedded in a textured Mg-matrix. Using this third approach, both hydrogen absorption and desorption kinetics are found to be markedly improved.

**Keywords**: Hydrogen storage; Fast forging; Hydrides; Microstructure; Texture; Magnesium.

**Corresponding authors:**

Dr. Jing WEN: jing.wen@neel.cnrs.fr

Dr. Patricia DE RANGO: patricia.derango@neel.cnrs.fr

## 1. Introduction

Magnesium and its alloys have gained a great interest in the field of hydrogen storage owing to their light weight, high hydrogen-storage capacity, low-cost and abundance in Earth's crust [1, 2]. In particular, Mg-based metal hydrides are still considered as one of the most promising solid-state hydrogen-storage media due to their higher energy density and safety advantages over the gas and liquid storage materials. However, the high thermodynamic stability of $MgH_2$ as well as the slow desorption kinetics limit the application of Mg-based hydride in industry [3, 4]. Efforts have been devoted to accelerate the absorption/desorption kinetics of Mg-based hydrides while lowering the temperature of reaction. This can be accomplished to some extent by modifying the microstructure of Mg-based hydrides. Fast sorption kinetics were achieved with nanosized $MgH_2$ powders produced by High Energy Ball Milling (HEBM) [5, 6]. Hydrogen diffusion is therefore accelerated owing to the increased density of grain boundaries, the larger reactive surface area and presumably a large amount of defects, although a recent review paper has outlined the limited understanding of the scientific community regarding the exact nature of structural defects and their effect [7]. However, HEBM cannot be applied to large-scale production due to energy, safety and processing time constraints.

To overcome these drawbacks, Severe Plastic Deformation (SPD) such as Equal Channel Angular Pressing (ECAP) [8-10], Cold Rolling (CR) [9,11] High Pressure Torsion (HPT) [12, 13] as well as Surface Mechanical Attrition Treatments (SMAT) [14, 15] have been recently employed to improve the H-storage properties through microstructure modifications. Additionally, a preferential texture is developed upon SPD, which has been reported to improve hydrogen absorption kinetics in AZ31 samples produced by ECAP and CR [10]. Forging is an alternative SPD route, which has been widely used for centuries in metallurgy. Compared to

ECAP, HPT and CR, forging is a simple, safe and cost-efficient approach to produce heavily deformed materials. According to the works of J. Huot [11] and A.C. Asselli [16], the hydrogen sorption kinetics of forged $MgH_2$ is similar to that observed in the samples produced by CR or HPT. However, large amounts of MgO formed as the number of forging passes increased, with a detrimental effect on the hydrogen absorption kinetics [16]. To avoid the formation of MgO upon multi-passes forging, single-pass fast forging (high deformation rate forging) under Ar atmosphere has been developed. Fast forging has also been shown to produce microstructures containing large amounts of defects as well as a preferential texture [17, 18], both leading to significantly modified sorption kinetics.

Among Mg-based alloys, $Mg_2Ni$ has been considered as one of the most promising hydrogen storage media owing to its favorable thermodynamics and relatively high hydrogen capacity [19, 20]. Upon hydrogenation at moderate temperature, $Mg_2Ni$ transforms into a ternary hydride $Mg_2NiH_4$ containing a hydrogen capacity of 3.6 wt.% [20]. In the present work, with the aim of enhancing the hydrogen storage performance of a Mg-based alloy (Mg-22 wt.% Ni), microstructure optimization through fast forging was investigated either at room or elevated temperatures. Moreover, annealing followed by fast cold forging was carried out to produce a specific microstructure characterized by fragmented $Mg_2Ni$ lamellae embedded in a textured Mg-matrix. The microstructure developed through fast forging was examined in the present work using a combined analysis of X-ray diffraction (XRD) and field emission scanning electron microscopy (SEM) coupled with electron backscatter diffraction (EBSD).

## 2. Experimental

The hypoeutectic composition Mg-22 wt.% Ni (equivalent to 78 wt.% Mg - 22 wt.% Ni) was selected to produce composites consisting of $Mg_2Ni$ domains embedded in a Mg matrix, by

refering to the Mg-Ni phase diagram. This composition is close to the Mg-rich eutectic at Mg-11.3 at.% Ni, but contains lower amount of Ni to avoid the formation of higher amount of $MgNi_2$ phase. Mg powder (atomized spherical particles of about 5 μm, 99.8% purity from SFM (Société pour la fabrication du magnésium; Switzerland) and nickel powder (30–40 μm, 99.5% purity from Neyco, France) were used as raw materials. Prior to fast forging, samples were prepared using the following procedures: firstly, a Mg-Ni mixture was fabricated by manual grinding of the Mg and Ni powders in a glove box under argon atmosphere; subsequently, the Mg-Ni pellets were compacted in a die using a 1 T/cm$^2$ press; finally, each sample containing 3 pellets (13 mm in diameter) was inserted into a thin cylindrical stainless steel sheath (22 mm in height) to avoid a burst effect of matter at shock [18]. The compacted powders in the form of pellets are referred as starting materials in the present work.

Plane-strain fast forging was performed at the laboratory scale using a device initially designed for hard magnets [17]. A 150 kg hammer is dropped from a height of 1.5 meters at a rate of 4.7 m/s onto a piston. The piston is in direct contact with the sample which is positioned on the anvil of a specially designed chamber. Three series of samples were prepared under argon atmosphere: 1) forged at room temperature (subsequently referred to as Cold forged, CF); 2) forged at the temperature of 450°C (referred to as Hot forged, HF); and 3) forged at room temperature after a preliminary annealing (referred to as Annealed + Cold forged, A + CF). Regarding the preliminary annealing, three pellets (inserted into a thin cylindrical stainless sheath) were heated by means of a retractable high frequency coil to 530 °C and maintaining for 30 minutes under Ar atmosphere. It should be noted that the temperature of the sheath gradually decreased as the annealing proceeded due to the increase of the electric conductivity of the sample; the final temperature was recorded as 455 °C. After fast forging, the height of the sample was reduced

from 75 % to 93 % (Table 2) depending on the forging conditions. The sample geometry before and after fast forging is shown in Fig. 1a.

Following fast forging, pieces were extracted from the center of the samples for microstructure characterizations, as illustrated in Fig. 1a. The sectioned faces were mechanical polished using SiC papers with grits from 1000 to 4000 followed by electrolytic polishing in an electrolyte of 62% phosphoric acid and 38% ethanol at 2V for 3 min, at -15 °C. Phase identifications were conducted on the horizontal polished surface using X-Ray Diffraction (XRD). The weight fraction of each phase component and the corresponding lattice strain were determined by Rietveld refinement using the FullProf suite [21]. Energy-dispersive X-ray (EDX) spectroscopy was employed to determine the chemical composition of the annealed sample. To collect the high-quality Kikuchi patterns, the samples were Ar ion polished with a PECS-II GATAN using 3.0 keV beam energy under dual beam condition, with gun angle of 2° and for about 3 hours. Then EBSD characterization was performed using a JEOL-6500F SEM equipped with the AZtec acquisition software package at a step size of 0.15-0.30 μm. In addition to the EBSD micro-texture measurements, XRD macro-texture measurements were carried out to have a better representation of the crystallographic texture of the fast forged samples. Totally, five pole figures $(0002)_{Mg}$, $(10\bar{1}0)_{Mg}$, $(10\bar{1}1)_{Mg}$, $(10\bar{1}2)_{Mg}$ and $(11\bar{2}0)_{Mg}$ have been measured and the texture components were recalculated using the ATEX software [22]. The hydrogen storage properties of the fast forged samples were examined using a Sievert device from HERA. Hydrogen absorption and desorption kinetics were measured at temperature of 310 °C under a hydrogen pressure of 20 bars and 1.5 bars, respectively. In total, 12 cycles of absorption/desorption were conducted for each forged sample.

## 3. Results and discussion

### 3.1 Structural and microstructural analysis

#### 3.1.1 Phase analysis

Phase composition was studied by XRD. Fig. 1b shows a comparison of the XRD patterns of the starting material Mg-22 wt.% Ni collected before and after annealing performed at 530°C under inert atmosphere for 30 min. A $Mg_2Ni$ phase formed by diffusion of Mg and Ni atoms during annealing. The weight fraction of $Mg_2Ni$ is determined to be 41 wt.% by Rietveld refinement, in agreement with the starting composition. Additionally, some weak diffraction peaks which correspond to the formation of small amounts of the $MgNi_2$ compound are observed. While $Mg_2Ni$ have formed by solid state diffusion of Ni within the Mg particles, the possibility of the formation of $MgNi_2$ by phase separation during local solidification, as previously reported by Ueda et al. [23], cannot be ruled out.

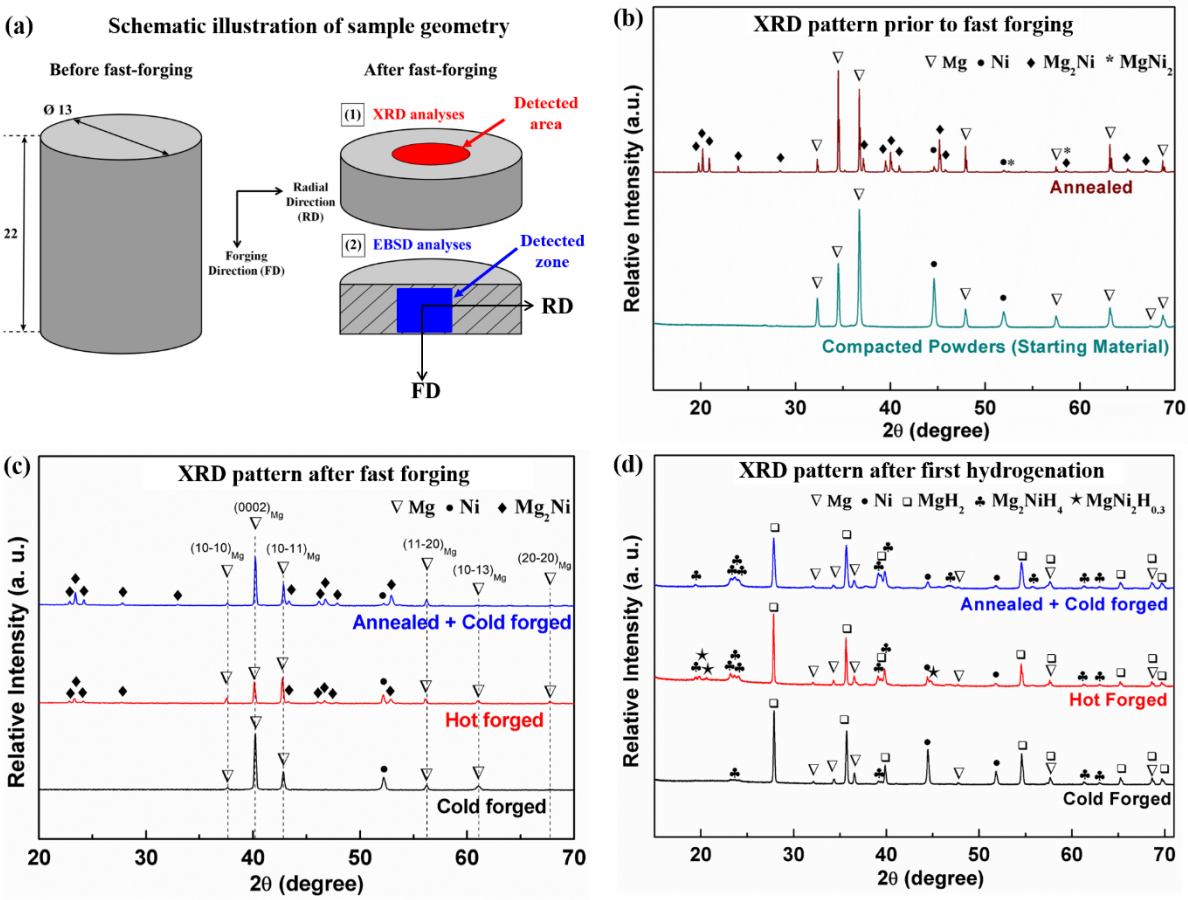


Fig. 1. Phase identification using XRD measurement. (a) Schematic of samples geometry and analyzed surfaces. Comparison of XRD patterns of (b) Starting material before and after annealing, (c) Cold forged, hot forged and annealed + cold forged samples, and (d) Cold forged, hot forged and annealed + cold forged samples after the first hydrogenation.

XRD patterns recorded on the as-forged samples are shown in Fig. 1c. For the CF sample, only the initial phases Mg and Ni were detected, indicating that no phase transformation occurs under the impact loading. Nevertheless, the relative high intensity of the $(0002)_{Mg}$ peak reveals that a basal texture is generated in the Mg phase upon the cold deformation. Regarding the HF sample, a $Mg_2Ni$ phase formed during the forging process. According to the Mg-Ni phase diagram, this intermetallic compound is expected to form at the eutectic temperature of 506˚C. Obviously, during fast forging, under the impact loading a part of the kinetic energy is converted into heat

which is dissipated in the sample. This stored energy might facilitate the formation of $Mg_2Ni$ below the eutectic temperature through an accelerated metal diffusion at the Mg/Ni interface. According to numerical simulation performed in Ref. [18], only one shock of forging resulted in an increase of temperature within the sample of 150-200 ˚C. Therefore, for the HF sample, with the assistance of the heat transformed from the kinetic energy, the real temperature of the sample overpassed the eutectic one, which enabled the formation of $Mg_2Ni$ at a local scale via fast alloying. For the A + CF sample, in addition to the relative high intensity of the $(0002)_{Mg}$ peak, broadening of the diffraction peaks is observed for both the Mg phase and the $Mg_2Ni$ intermetallic compound due to the generation of lattice strain upon cold forging.

The weight fraction of each phase and the corresponding lattice strain, extracted from Rietveld refinements are presented in Table 1 and Table 2, respectively. The estimated weight fractions of Mg and Ni in the CF sample are consistent with the ones we designed. Nevertheless, a higher extent of lattice strain is generated in the CF samples. For the HF sample, a very low fraction (~ 2.22 wt. %) of Ni retained in the sample implies that Ni is not completely consumed upon the formation of $Mg_2Ni$. This could be due to either the inhomogeneous distribution of heat within the sample or the size effect of the Ni particle [24].

Table 1: Weight fraction of each phase component in annealed and as-forged samples.

| Sample series | Forging temperature (°C) | Weight fraction (wt. %) | | |
|---|---|---|---|---|
| | | Mg | Ni | $Mg_2Ni$ |
| CF | 25 | 78.22 ± 2.07 | 21.78 ± 2.06 | - |
| HF | 450 | 62.36 ± 1.50 | 2.22 ± 0.78 | 35.42 ± 2.02 |
| Annealed (530°C) | - | 56.85 ± 2.30 | 1.50 ± 0.16 | 41.65 ± 1.95 |
| A + CF | 25 | 57.75 ± 2.89 | 1.40 ± 0.17 | 40.85 ± 1.95 |

Table 2: Thickness reduction ratios and lattice strain of each phase in annealed and as-forged samples.

| Sample series | Reduction ratio (%) | Lattice strain (%) | | |
|---|---|---|---|---|
| | | Mg | Ni | $Mg_2Ni$ |
| CF | 79.0 | 0.14 ± 0.01 | 0.18 ± 0.01 | - |
| HF | 93.0 | 0.09 ± 0.01 | 0.08 ± 0.01 | 0.05 ± 0.01 |
| Annealed (530°C) | - | 0.08 ± 0.01 | 0.05 ± 0.01 | 0.06 ± 0.02 |
| A + CF | 75.0 | 0.16 ± 0.01 | 0.13 ± 0.01 | 0.08 ± 0.02 |

After the first hydrogenation, the forged samples are based on three major phases: $MgH_2$ (tetragonal), $Mg_2NiH_4$ (monoclinic) and metallic Mg indicating that the hydrogenation is incomplete (Fig. 1d). Also the observation of $Mg_2NiH_{0.3}$ reveals that some of the hydrogen atoms are dissolved as a solid solution within the $Mg_2Ni$ lattice.

Only a small amount of the $Mg_2NiH_4$ hydride is observed in the CF sample and most of the nickel remains as metallic Ni particles. In contrast, the quantity of $Mg_2NiH_4$ hydride is quite high for the forged samples containing the $Mg_2Ni$ phase (A + CF and HF). Moreover, we noticed that a peak appears between the doublet of $Mg_2NiH_4$ in the XRD pattern at about 23-24º. These reflections can be assigned to stacking faults in $Mg_2NiH_4$ [25, 26], which can act as quick pathways for the transportation of hydrogen [27].

3.1.2 Texture development upon fast forging

Since plastic deformation is dominated by magnesium for the powder mixture of Mg-22 wt.% Ni, the texture development of Mg upon fast forging was examined using XRD, as shown in Fig. 2, where the recalculated (0002) and (10-10) pole figures are presented. For the CF sample (Fig. 2a),

a fiber texture characterized by a majority of c-axes approximately aligned with the forging direction is developed under forging. The formation of this {0001} basal fiber texture is related to the slip systems $\{0001\}<11\bar{2}0>$ operating on the basal planes [28]. Regarding the HF sample (Fig. 2b), the {0001} texture intensity has been weakened due to the occurrence of dynamic recrystallization upon hot deformation. With respect to the A + CF sample (Fig. 2c), the texture intensity is comparatively lower than that for the CF sample. Keeping in mind that the intensity of texture is proportional to the volume fraction of grains having a preferential crystallographic orientation, this lower fraction can be explained by differences in the fine scale deformation mechanisms due to the composite nature of the deformed materials containing hard $Mg_2Ni$ particles.

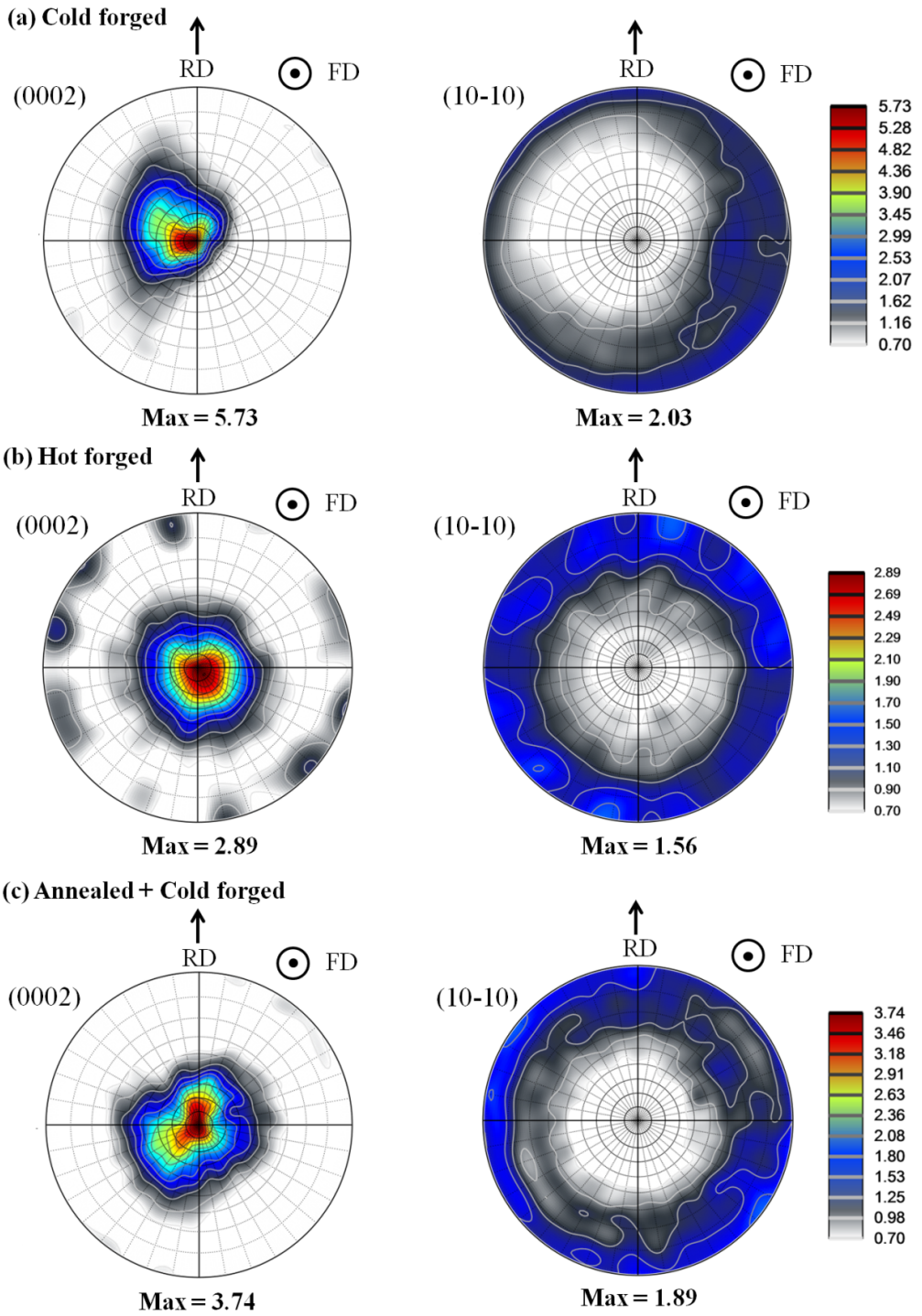


Fig. 2. Pole figures of (0002) and (10-10) for Mg-phase measured using XRD: (a) CF, (b) HF and (c) A+ CF. (RD: radial direction).

3.1.3 Microstructure analysis of the cold forged (CF) sample

EBSD technique was used to investigate the microstructure evolution upon cold forging of the CF sample (Fig. 3). As illustrated in the schematic drawing in Fig. 1a, EBSD measurements have been carried out on a cross-section along the forging direction (FD). In the inverse pole figure (IPF) map of Fig. 3a, the Mg grains are colored while the Ni phase remains in white. The majority red color of the Mg grains indicates that they globally exhibit a preferential orientation (texture). Indeed, in agreement with the macro-texture determined by XRD (Fig. 2a), the (0002) pole figure in Fig. 3b, which corresponds to the IPF map, confirms the presence of a fiber texture with a majority of grains in the CF sample having <0001> directions approximately parallel to the forging direction.

Fig. 3c shows an IPF map (corresponding to the selected zone in Fig. 3a) of the Mg grains superimposed with their grain boundaries taken at a smaller step size of 0.10 μm, in which the high and low angle boundaries are outlined by black and grey colors, respectively. According to Ref. [29], high-angle boundaries (HABs) are identified with a minimum of 15° misorientation angle across the grain boundaries. Low-angle boundaries (LABs) are defined with misorientation angle below 15°. Due to the experimental error in evaluating orientations by EBSD [30], grain boundary misorientations below 2° are excluded from the data analysis. As seen, the grain boundaries of magnesium are decorated with high angle boundaries, whereas the interior of that is filled with low angle boundaries. Fig. 3d shows the IPF map of Ni-phase corresponding to the selected zone in Fig. 3a. The Ni grains, with size less than 1 μm, are distributed within the Mg matrix in the form of agglomerations.

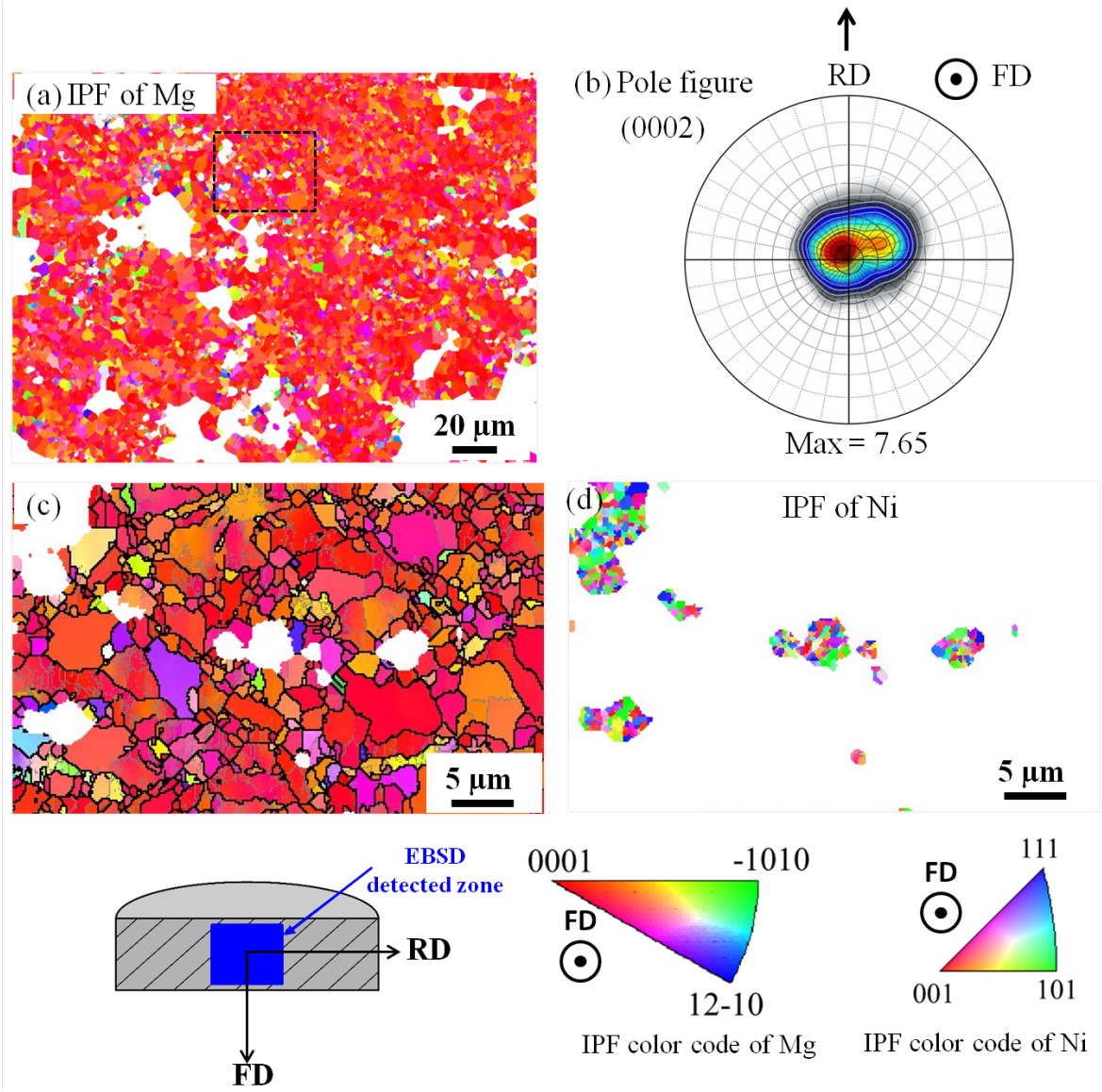


Fig. 3. EBSD characterization taken from the cross-section of CF sample: (a) IPF map of Mg-phase, Ni indicated by white color, (b) (0002) pole figure, (c) IPF map superimposed with grain boundary corresponding to the selected zone in (a) taken at a smaller step size and (d) IPF map of Ni corresponding the selected zone in (a). High and low angle grain boundaries are indicated by black and grey, respectively.

Grain size distribution as well as grain/sub-grain boundary misorientation distributions obtained from the analysis of EBSD maps taken on the different samples are shown in Fig. 4. The LogNormal function, which is often used to describe grain size distribution in polycrystals, has

been fitted to the grain size distribution (in terms of area fraction). The analysis shows that the cold forged sample has a rather wide range of Mg grain size lying within the range ~ 1–10μm (Fig. 4a). As for the Mg-phase misorientation angle distribution in the CF sample, the black line in Fig. 4b indicates the random distribution of misorientation angle expected for hexagonal structure without any texture [31], often referred as Mackenzie distribution. Because of the presence of a fiber texture in which many grains have a common crystallographic axis parallel to the forging direction, the 2D misorientations between adjacent grains are generally of lower magnitude in the forged samples than the expected ones in a material having a random orientation of grains (no texture).

For comparison, the grain size distributions for HF and A + CF samples are also given in Fig. 4. The HF specimen contains mostly fine Mg grains ranging within the 1 to 6 μm size range with an average size of ~2.7 μm, as shown in Fig. 4c. The newly formed $Mg_2Ni$ intermetallic compound is composed of fine to coarse grains ranging from ~1 to 10 μm in size (Fig. 4d). For the A + CF sample, because of some grain growth during pre-annealing, there is a more pronounced heterogeneity in Mg-grain size, as depicted in Fig. 4e. Due to the "fragmentation" of the brittle $Mg_2Ni$ domains upon cold forging, the $Mg_2Ni$ grains are slightly finer: 2.6 μm for the A + CF condition (Fig. 4f) compared to 3.7 μm for the HF sample (Fig. 4d).

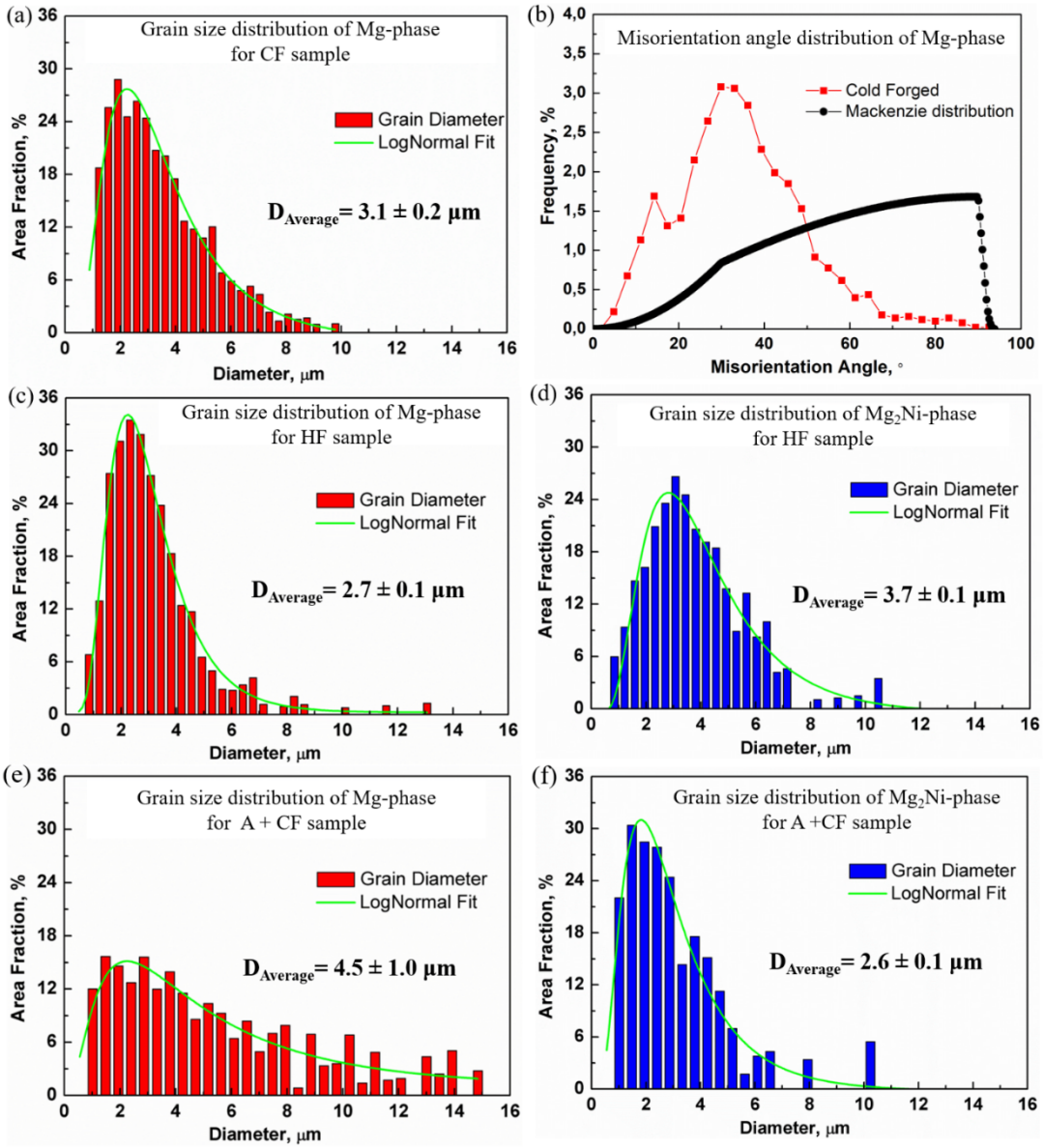


Fig. 4. Grain size distributions of Mg-phase for CF (a), HF (c) and A + CF (e) samples. Misorientation angle distribution of Mg-phase for CF sample (b). Grain size distributions of $Mg_2Ni$ for HF (d) and A + CF (f) samples.

### 3.1.4 Microstructure analysis of the hot forged (HF) sample

The microstructure of the HF sample was investigated using SEM-EBSD measurement performed on cross-section of the sample. Fig. 5a shows an EBSD phase map superimposed with

a band contrast, where the Mg, $Mg_2Ni$ and Ni phases are revealed in red, blue and yellow colors, respectively. Figs. 5b, 5c and 5d present the IPF map of the Mg, $Mg_2Ni$ and Ni phases, respectively. Absent in the cold forged sample, randomly orientated $Mg_2Ni$ grains having a fairly equiaxed shape have formed in the Mg-matrix during the hot forging process. The enthalpy of formation of $Mg_2Ni$ arises from the external heat as well as the additional heat transformed from the impact loading. As shown in Fig. 5e, a SEM-SEI image taken at higher magnification corresponding to the selected area in Fig. 5a, there are Ni particles dispersed close to the newly formed $Mg_2Ni$ grains, which indicates that the initial mixed Mg/Ni powders were not fully transformed into $Mg_2Ni$. This could result from either the inhomogeneous distribution of heat within the sample volume or the size effect of the Ni particles [24]. Ni grains with an average size of 800 nm are retained in the hot forged sample as a result of the short reaction time at high temperature which does not allow full alloying with Mg. Dynamic recrystallization has occurred during the thermo-mechanical processing of this hot forging, which affects the evolution of the microstructure like grain size, texture and stored energy etc. [32-36]. Examples of recrystallized $Mg_2Ni$ and Ni grains are indicated by blue and yellow markings in Fig. 5e. Indeed, primary recrystallization is a mechanism operating by a nucleation and growth process. While it is well established that the nuclei are regions that already exist in the deformed microstructure, the growth stage requires a sufficient misorientation between these nuclei and the deformed grains that they are consuming to develop [28, 37]. This inevitably generates a weakening of the deformation texture [37].

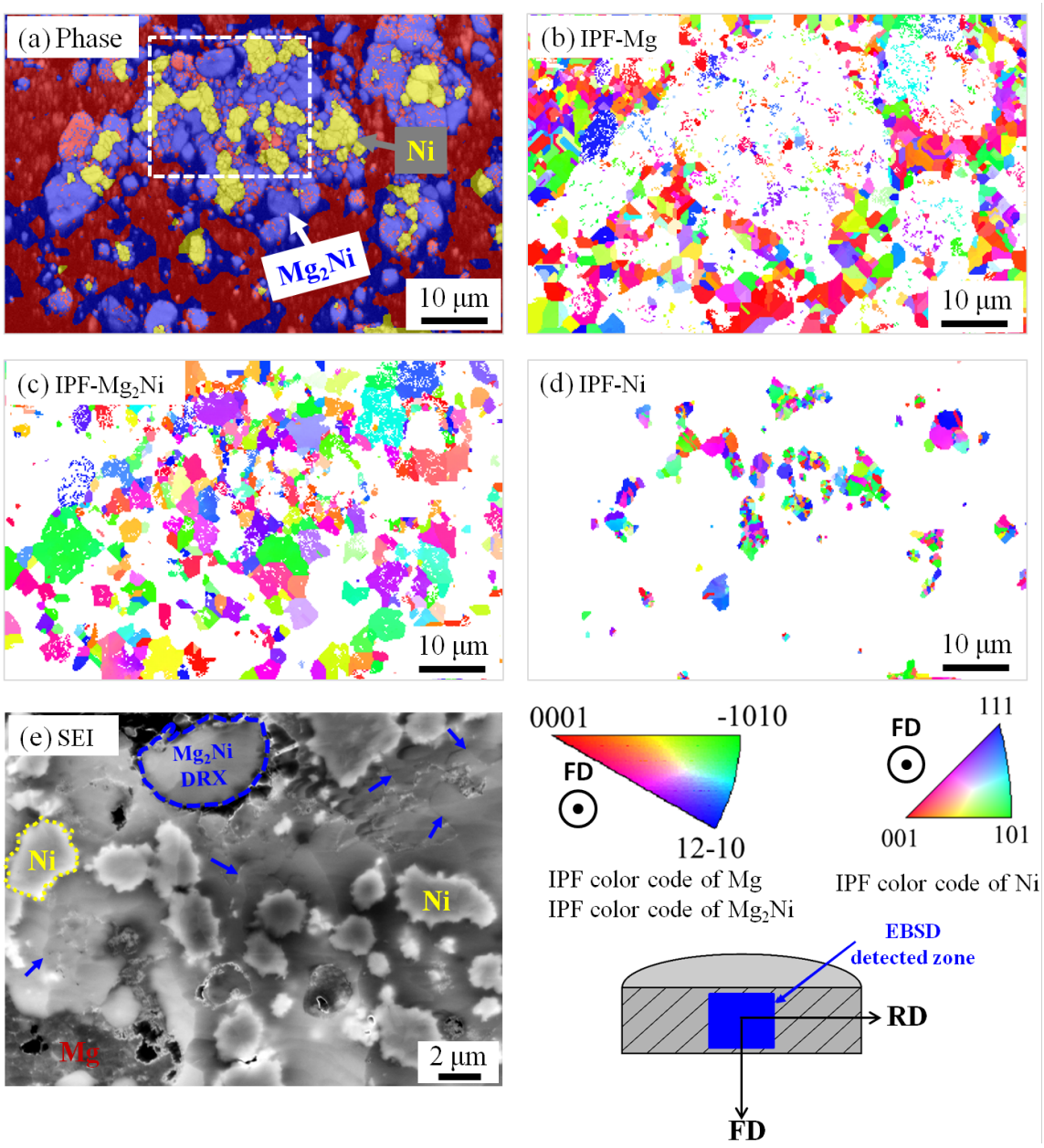


Fig. 5. SEM-EBSD characterization taken from the cross-section of HF sample: (a) EBSD phase map superimposed with band contrast, in which the phases Mg, $Mg_2Ni$ and Ni are indicated by red, blue and yellow, respectively; IPF maps of Mg (b), $Mg_2Ni$ (c) and Ni (d), respectively; and (e) SEM-SEI image corresponding to the selected area in (a).

3.1.5 Microstructure analysis of the annealed and cold forged (A + CF) sample

The morphology and chemical analysis of the annealed mixed powder Mg-22 wt.% Ni was characterized using SEM-EDX analysis prior to forging. Micrographs shown in Fig. 6a and Fig 6c (the latter being a magnification of the selected area 3 of the former) reveal that upon annealing, some Mg particles (initially rounded) have evolved into more angular and faceted Mg grains, in the form of octahedral truncated shape (see pink arrow in Figs. 6a), whereas some larger Mg particles remained rounded (see white arrow in Fig. 6c).

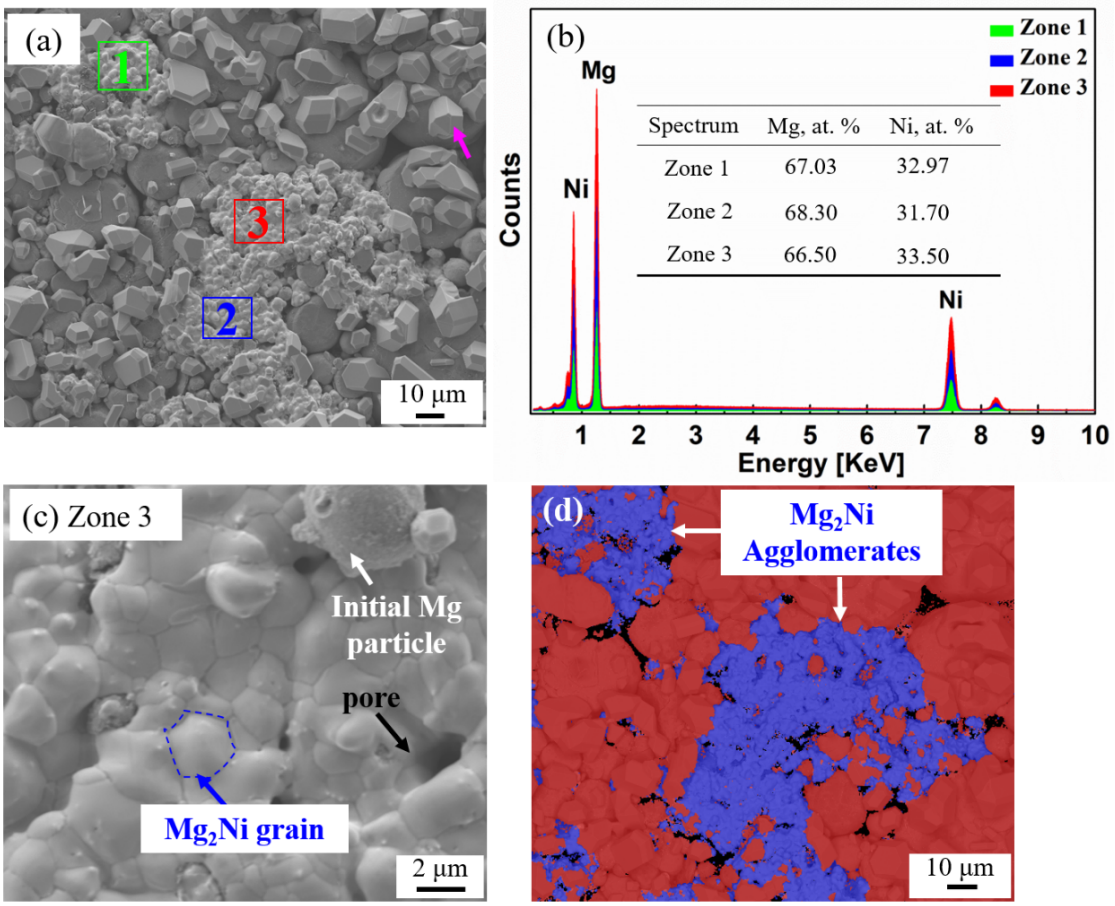


Fig. 6. Microstructure of the annealed Mg-22 wt. % Ni, (a) SEI image; (b) EDX spectrum taken from three different areas 1, 2 and 3, as indicated by the rectangles in (a); (c) zone 3 at higher magnification and (d) superimposed map of the elements distribution (Mg and $Mg_2Ni$ indicated by red and blue, respectively.)

EDX spectrum taken in three different areas, as indicated by the rectangles labeled 1, 2 and 3 in the SEM-SEI image (Fig. 6a) are displayed in Fig. 6b. The chemical compositions measured in the three areas are also given in Fig. 6b. The measured atomic ratios of Mg to Ni are nearly equal to the theoretical values (2:1), which further confirms the formation of $Mg_2Ni$ during annealing. Fig. 6d shows the superimposed map of the elements distribution using Mg-K and Ni-L. As observed, the newly formed $Mg_2Ni$ phase exists as agglomerates in the Mg matrix. This is due to the fact that in the process of annealing, the Mg and Ni atoms diffuse across the boundaries of the initial particles, fusing the particles together and creating recrystallized $Mg_2Ni$ grains (Fig. 6c). The grain size of $Mg_2Ni$ ranges from hundreds of nanometers to several micrometers. Additionally, it can be noticed that pores are distributed in the formed $Mg_2Ni$, as indicated by the black arrow in Fig. 6c. Indeed, in the present work, annealing of the mixture powders of Mg-22 wt.% Ni can be considered as a sintering process. Since the material is seeking to lower its surface energy by moving atoms toward the points of contact between particles, the contact points become larger and eventually $Mg_2Ni$ agglomerates containing small pores are created during annealing/sintering.

Fig. 7a and Fig. 7b show cross section micrographs of the A + CF sample at different magnifications. As observed, the equiaxed $Mg_2Ni$ grains (Fig. 7c) became fragmented lamellae after fast cold forging. The thickness of the lamellae ranges from several tens of nanometers to several micrometers. The fragmentation of $Mg_2Ni$ upon fast cold forging is expected since it cannot accommodate the imposed plastic strain due to the brittle nature of this intermetallic compound. Obviously, a considerable amount of cracks was generated in the interior of the $Mg_2Ni$ intermetallic compound, as indicated by the black arrows in Fig. 7b. These cracks, can act as hydrogen diffusion paths.

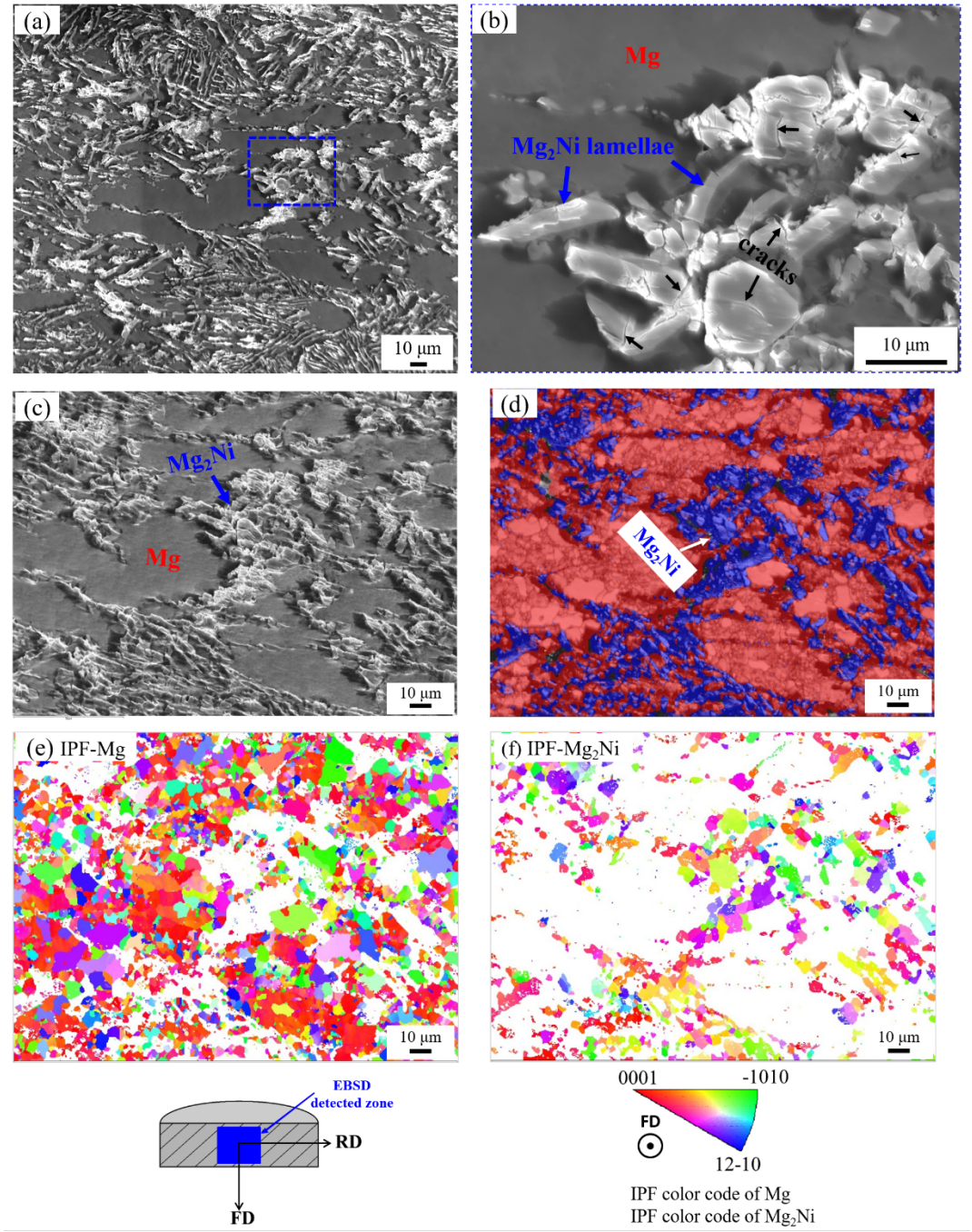


Fig. 7. SEM-EBSD characterization of A + CF sample. SEM-SEI images taken from the cross-section (a) and zoom of the selected area (b); SEM-BSE image (c); phase map superimposed band contrast in which Mg and $Mg_2Ni$ are indicated by red and blue, respectively (d). IPF maps of Mg (e) and $Mg_2Ni$ (f), respectively.

Numerous studies have reported that $Mg_2Ni$ in the form of lamellae or nanoparticles can enhance the hydrogen sorption properties owing to the accelerated hydrogen diffusion through the interface between Mg and $Mg_2Ni$ [38-45]. In the present work, Mg/$Mg_2Ni$ interfaces result from the embedding of fragmented $Mg_2Ni$ lamellae in the Mg-matrix, as revealed by the Backscattered-Electron (BSE) image in Fig. 7c. This peculiar microstructure is confirmed by the chemical analysis obtained from EBSD phase map superimposed with band contrast (Fig. 7d), in which the Mg and $Mg_2Ni$ phases are indicated by red and blue, respectively. The Mg phase exhibits some extent of a preferential grain orientation with respect to the forging direction with the classic {0001} fiber texture (see IPF map of the Mg and $Mg_2Ni$ phases in Figs. 7e and 7f respectively), as was confirmed by the XRD macro-texture measurement shown in Fig. 2c. This is due to the fact that the deformation incompatibility between the Mg-matrix and the hard $Mg_2Ni$ intermetallic compound hinders the reorientation of the Mg-grains with respect to forging direction. Moreover, this plastic strain incompatibility induces a considerable amount of cracks in the hard $Mg_2Ni$ particles. Subsequently, as will be confirmed hereafter from the H-storage data, these cracks can act as quick pathways for the hydrogen transportation in the A + CF sample.

## 3.2 Hydrogen storage performance

### 3.2.1 Sample activation

Sample activation refers to the first hydrogenations of the material. It usually occurs very slowly in “standard” micrometric Mg powders. The weak activation rate constitutes an important limitation on the use of Mg- rich alloys for hydrogen storage. Without a tailored microstructure, first hydrogenation of Mg powders requires typically 24h at 400°C under 30 bars of hydrogen [3, 46]. In this study, hydrogenation of all samples was carried out at 310°C under a hydrogen

pressure of 20 bars. A comparison of the hydrogen uptakes recorded for fast forged samples as well as for compacted powders (starting materials) is shown in Fig. 8a. The beneficial effect of the peculiar microstructure developed upon cold forging is noticeable with fastest hydrogenations - without any incubation time - and highest uptakes recorded for both CF and A + CF samples. The basal fiber texture as well as a considerable amount of cracks induced upon cold forging may facilitate hydrogen diffusion through the samples leading to faster absorption rates than the one observed for the starting materials. Our results are in line with the work of Jorge Jr et al. [10], who showed that the fiber texture is the best orientation for hydrogen absorption. Structural defects like dislocations, grain boundaries, twins and stacking faults produced by the severe plastic deformation are likely to create diffusion paths and increase the surface reactivity, thereby improving hydrogen sorption kinetics of magnesium-based alloys [10-16, 27]. On the other hand, the hot forged sample exhibited the slowest absorption kinetics and the lowest hydrogen uptake capacity (~1 wt.% of hydrogen) after 2 hours of hydrogenation due to the weaker basal fiber texture, the lower amount of structural defects and the absence of any porosity and cracks within the sample. The compacted powder displays a relatively fast absorption owing to the facile hydrogen diffusion between the less compacted particles.

Interestingly, a two-stage hydrogen activation is observed for the CF sample: a fast absorption occurs at the very beginning of the reaction followed by a gradual stabilization and a hydrogen uptake of about 1.2 wt.%. After 50 minutes the uptake absorption kinetics goes again through a strong increase leading to an uptake of about 6 wt.% after 6.5 hours (curve not shown). The apparent limited maximum uptake is due to a deliberate choice to stop the experiment. As it has been checked also for the A + CF sample, a full hydrogenation of the samples is achieved for longer time. Regardless of the proportion of Mg alloyed with nickel, the theoretical hydrogen

gravimetric capacities for the HF, CF and A + CF samples are 5.93 wt.%. Thus no significant loss of hydrogen capacity is detected. Moreover, the phenomenon of hydrogen trapping by lattice defects, such as grain/phase boundaries and dislocations [47, 48] cannot be evidenced due to the experimental resolution. To understand the kinetics mechanism behind this two-stage hydrogen absorption, two general kinetic models, Jonhson-Mehl-Avrami-Kolomogorov (JMAK) model [49] and Jander model [50], have been used to fit the isothermal data. However, the obtained data cannot be fitted with any of these models, even the improved classical nucleation-growth-impingement mode (C-JMAK) recently proposed by Pang et al. [51]. This means that the kinetic mechanisms responsible for this two-stage hydrogen absorption cannot be solely determined by kinetic models. One possible explanation may arise from the phase composition. XRD patterns (Fig. 1c) have shown that the CF sample is only composed of elemental Mg and Ni while additional $Mg_2Ni$ alloy is visible in the A + CF sample. This difference in phase distribution may explain the unlike absorption profiles between CF and A + CF samples. In the A + CF sample, the already formed $Mg_2Ni$ contributes to the fast kinetics of the first hydrogenation, while only interfaces between Mg and Ni particles can be part of the kinetics enhancement in the CF sample. After completion of the first hydrogenation, Ni is partly alloyed with Mg (as shown in XRD pattern Fig.1d and the two stage behavior is no more visible (Fig. 8c). The present experimental observations are in line with previous reports that describe sorption mechanisms in Mg-Ni alloys. According to Refs [52,53], hydrogenation starts with the dissolution of hydrogen atoms into $Mg_2Ni$ towards the formation of the $Mg_2NiH_{0.3}$ solid solution, and, in a second stage, the magnesium hydride appears. The ternary hydride $Mg_2NiH_4$ crystallizes as soon as the hydrogen content in $Mg_2NiH_{0.3}$ reaches saturation.

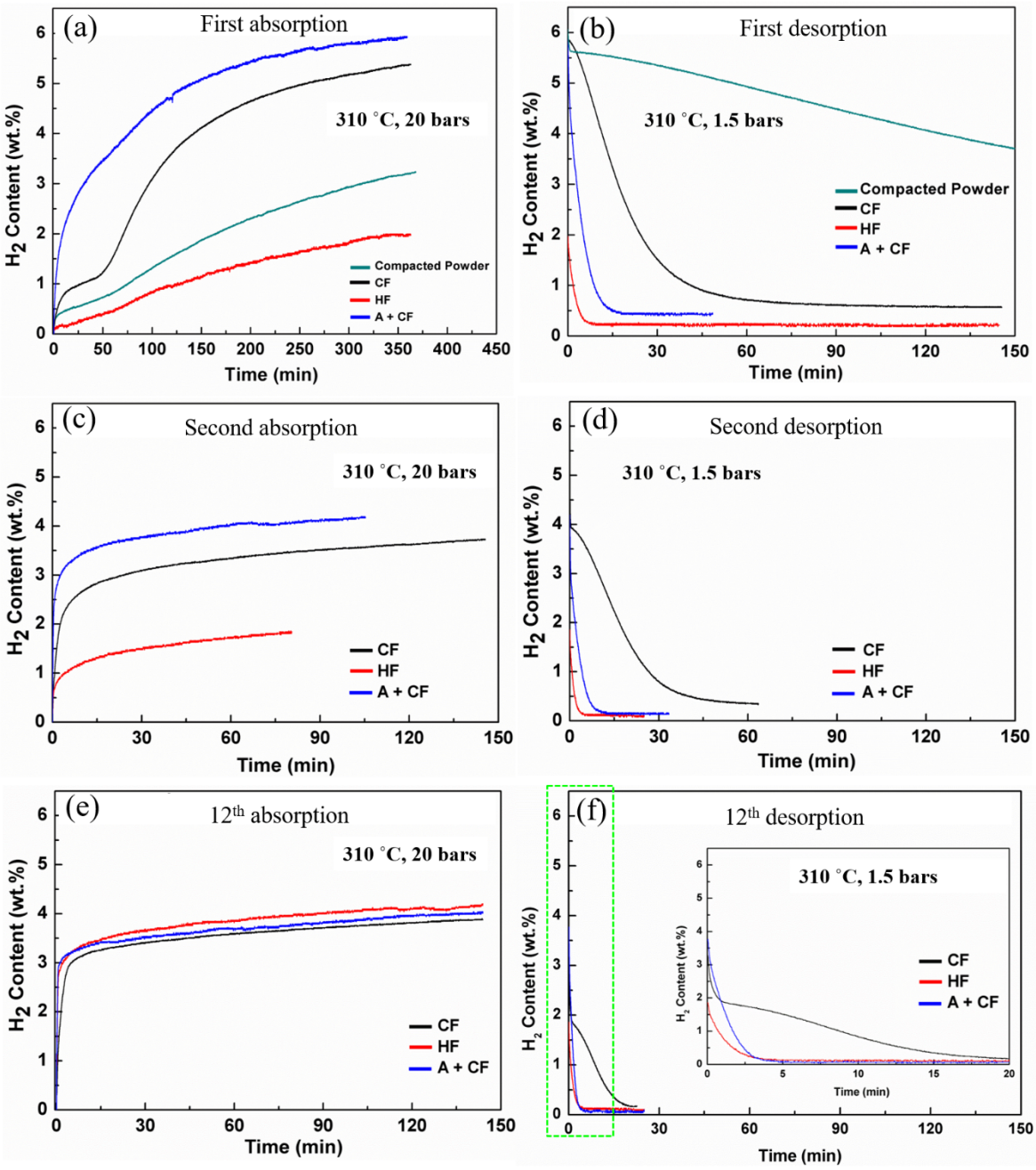


Fig. 8. Hydrogen sorption curves for different cycles. Absorption was performed at 310 ˚C, 20 bars and desorption at 310 ˚C, 1.5 bars. First (a), second (c) and 12$^{th}$ (e) absorption steps; first (b), second (d) and 12$^{th}$ (f) desorption steps. Absorption measurements were intentionally stopped after 80 min, 110 min or 140 min to limit the acquisition duration.

### 3.2.2 Role of $Mg_2Ni$ on desorption kinetics

Hydrogen release curves that correspond to the first desorption (measured at the temperature of 310 °C under a pressure of 1.5 bars) for the three fast forged samples as well as the starting material are gathered in Fig. 8b. As anticipated, the compacted powders show a very slow desorption kinetics (10 hours are needed to achieve full desorption), which is due to the high stability of the $MgH_2$ hydride [5-7, 52] as well as the slow diffusion of hydrogen through the $MgH_2$ hydride phase. Interestingly, a rapid desorption occurred in both HF and A + CF samples whereas CF sample features a slower dehydrogenation rate. We assign this significant difference to the phase content. In fact, as determined by Rietveld refinement in section 3.1.1, the HF and A + CF samples contain large amount of $Mg_2Ni$ –phase, whereas this intermetallic is absent in the as forged CF sample. The faster desorption kinetics in the samples that contain the $Mg_2Ni$ phase can be directly attributed to the lower/weaker stability of the hydride phase $Mg_2NiH_4$ that facilitates the hydrogen release upon desorption. According to Refs. [52, 53], during desorption, the ternary hydride $Mg_2NiH_4$ is first decomposed into the $Mg_2NiH_{0.3}$ phase due to its higher hydrogen chemical potential. After that, the stable hydride $MgH_2$ starts to decompose into Mg and hydrogen. Additionally, as mentioned above, stacking faults have formed within the structure of the monoclinic $Mg_2NiH_4$ hydride. Similar to grain boundaries and cracks, these stacking faults can act as fast pathways to transport hydrogen from the interior of samples to the outer surface. Nevertheless, it is worth to mention that hydrogen was not fully released from the hydrogenated samples after the first desorption, as revealed in Fig. 8b, which is associated with the remaining hydrogen atoms present in solid solution $Mg_2NiH_{0.3}$.

### 3.2.3 Hydrogen sorption kinetics after activation

Successive absorption/desorption kinetics were measured under conditions similar to the one used for activation. Fig. 8c shows the hydrogen absorption kinetics recorded at the second cycle for the forged samples. Since these samples were partly activated after the first cycle, the second absorption kinetics was remarkably improved for all the forged samples (Fig. 8c). Nevertheless, the hot forged sample still displays the slowest absorption kinetics due to the lack of any porosity and/or cracks for hydrogen penetration. Fig. 8d displays the hydrogen desorption kinetics recorded at the second cycle. The hydrogen desorption kinetics has improved to some extent for all the forged samples, despite the CF sample which still exhibits the slowest desorption behavior. Although the sorption cycles can be treated as annealing processes to homogenize the microstructure, the sluggish desorption observed in the CF sample reveals that the amount of Ni alloyed with Mg remains low and $Mg_2Ni$ content is poor after two cycles of sorption.

After 11 sorption cycles, all the samples display similar absorption curves, with a markedly fast kinetics during the first 5 minutes followed by a strong slowdown, as depicted in Fig. 8e. The observations may indicate that the absorption/desorption cycles - and the associated volume changes and consequent lattice strain - have modified the initial microstructures to reach a "normalized" structure rather identical to all the 3 samples. Several modifications can take place under cycling such as recovery / recrystallization, grain growth, fragmentation of the samples - associated to the volume changes under hydrogenation - to form fine powder particles, re-annealing of these powder particles, etc. [9, 12]. This generates a microstructure of cycled materials that depends less on the initial processing, which is however essential to improve the first hydrogenation. Whereas the unified microstructure leads to fast hydrogen absorptions for all three samples, the desorption kinetics of the CF sample remains low compared to the HF and A + CF samples even after 11 cycles (see Fig. 8f). The dehydrogenation curve of CF sample remains

quasi identical from the first to the 12 following desorptions suggesting that the catalytic phase $Mg_2NiH_4$ is not in sufficient quantity or in adequate distribution in the cold forged sample despite several cycles.

It is interesting to note that a two-stage hydrogen desorption is even observed for the three samples as depicted by the insert in Fig. 8f. The fast desorption at the first stage can be attributed to a rapid decomposition of the $Mg_2NiH_4$ hydride. The slower desorption kinetics at second stage can be then ascribed to the slow release of H from the stable $MgH_2$ hydride. The further analysis of the kinetic mechanisms involved in absorption/desorption investigated by in-situ neutron diffraction is in progress and will be reported later.

Table 3 Comparison of hydrogen sorption properties of Mg-Ni samples obtained in the present work and from literature [41, 43].

| Sample | Techniques | Sorption temperature (°C) | Absorption pressure (bars) | Desorption pressure (bars) | Max uptake after 1st absorption (wt.%) | H retained after 1st desorption (wt.%) |
|---|---|---|---|---|---|---|
| Mg-22 wt.% Ni (this work) | CF | 310 | 20 | 1.5 | 5.8 | 0.80 |
| | HF | | | | 2.0 | 0.25 |
| | A + CF | | | | 6.0 | 0.70 |
| $Mg_{75}Ni_{25}$ Mg-45 wt.% Ni [41] | HEBM + HPT | 300 | 10 | 0.1 | 3.0 | 0.45 |
| $Mg_{75}Ni_{25}$ Mg-45 wt.% Ni [43] | HEBM | 300 | 10 | - | 2.4 | - |
| | HEBM + ECAP | | | | 1.5 | - |
| | HEBM + CR | | | | 2.4 | - |

Table 3 summarizes the H-storage properties of the Mg-Ni powders obtained by fast forging in the present work and by different SPD routes from the literatures [41, 43]. Regarding the chemical composition of Mg-Ni powder, a lower amount of Ni contained in the current samples

(Mg-22 wt.% Ni) leads to a theoretical hydrogen capacity of 5.97 wt. %, as compared to 4.2 wt. % for the (Mg-45 wt.% Ni) one employed in Refs. [41, 43]. Without considering the effect of absorption pressure, the hydrogen storage capacity is significantly increased for the sample prepared by annealing and fast cold forging, as compared to the maximum hydrogen uptake achieved for the sample prepared by combination of HEBM and HPT, which remains lower than expected (3.0 wt.% instead of 4.2 wt.%). For the starting material made by HEBM, the maximum hydrogen uptake is evidently promoted by HPT, whereas it is decreased by 35% through 6 passes of ECAP or one pass of CR [43]. Interestingly, after 10 passes of CR, the maximum hydrogen uptake is identical to the initial value (2.4 wt.%) recorded for the HEBM sample. These differences could result from the distinct extents of shear strain imposed by the different SPD modes [43]. The multi-passes SPD often generates a preferential texture that promotes hydrogen absorption, however, the absence of any porosity retards hydrogen penetration from surface into bulk [8]. The enhanced hydrogen storage performance achieved in this work is due to the co-existence of a preferential fiber texture and amounts of the cracks, the interfaces and the structural defects. The primary advantage associated the fast cold forged sample subjected to pre-annealing is the generation of considerable amounts of cracks accompanied with the fragmentation of the $Mg_2Ni$ lamellae, which act as hydrogen diffusion paths from surface through bulk.

## 4. Conclusions

The aim of the present work was to improve our understanding of microstructure modifications (including nature of phases and structural defects, grain sizes and texture) on the H-storage behavior in Mg-based composites (Mg -22 wt.% Ni). In terms of activation (i.e. first absorption), it appears that a stronger {0001} Mg fiber texture formed during cold deformation as well as the

presence of structural defects and micro-cracks in the processed samples are beneficial since they create easier propagation paths for H diffusion within the bulk of the sample. Regarding the desorption behavior, the best desorption kinetics were obtained in the presence of the $Mg_2Ni$ phase due to the weaker stability of the $Mg_2NiH_4$ hydride phase which favors the H release upon desorption. A consequence of these observations in terms of optimal processing to create a material having both an improved absorption as well as an improved desorption is the A + CF processing route that generates the formation of a cracked microstructure combining fine grains of $Mg_2Ni$ phase (favorable for desorption) and textured Mg grains (favorable for absorption).

**Acknowledgement**

The authors appreciate the financial support from the IDEX-CDP Eco-SESA program, from the University Grenoble Alpes, France. This work was also supported by the French State through the program "Investment in the future" operated by the National Research Agency (ANR) and referenced by ANR-11-LABX-0008-01 (Labex DAMAS).

**References**

[1] B. Sakintuna, F. Lamari-Darkrim, M. Hirscher, Metal hydride materials for solid hydrogen storage: a review, Int. J. Hydrogen Energy 32 (2007) 1121-1140.

[2] I.P. Jain, C. Lal, A. Jain, Hydrogen storage in Mg: a most promising material, Int. J. Hydrogen Energy 35 (2010) 5133-5144.

[3] A. Zaluska, L. Zaluski, J.O. Ström-Olsen, Nanocrystalline magnesium for hydrogen storage, J. Alloys Compds. 288 (1999) 217-225.

[4] G. Barkhordarian, T. Klassen, R. Bormann, Effect of $Nb_2O_5$ content on hydrogen reaction kinetics of Mg, J. Alloys Compds. 364 (2004) 242-246.

[5] J. Huot, G. Liang, S. Boily, A. van Neste, R. Schultz, Structural study and hydrogen sortion kinetics of ball-milled magnesium hydride, J. Alloys Compd. 293–295 (1999) 495-500.

[6] J.L. Bobet, B. Chevalier, M.Y. Song, B. Darriet, J. Etourneau, Hydrogen sorption of Mg-

based mixtures elaborated by reactive mechanical grinding, J. Alloys Compds. 336 (2002) 292 - 296.

[7] J. Huot, F. Cuevas, S. Deledda, K. Edalati, Y. Filinchuk, T. Grosdidier, B.C. Hauback, M. Heere, T.R. Jensen, M. Latroche, S. Sartori, Mechanochemistry of metal hydrides: recent advances, Materials 12 (2019) 2778.

[8] A.M. Jorge Jr, E. Prokofiev, G.F. Lima, E. Rauch, M. Veron, W.J. Botta, M. Kawasaki, T.G. Langdon, An investigation of hydrogen storage in a magnesium-based alloy processed by equal-channel angular pressing, Int. J. Hydrogen Energy 38 (2013) 8306-8312.

[9] L. Popilevsky, V.M. Skripnyuk, Y. Estrin, A. Dahle, D. Mirabile Gattia, A. Montone, E. Rabkin, Hydrogenation-induced microstructure evolution in as cast and severely deformed Mg-10 wt.% Ni alloy, Int. J. Hydrogen Energy 38 (2013) 12103-12114.

[10] A.M. Jorge Jr, G.F. de Lima, M.R. Martins Triques, W.J. Botta, C.S. Kiminami, R.P. Nogueira, A.R. Yavari, T.G. Langdon, Correlation between hydrogen storage properties and textures induced in magnesium through ECAP and cold rolling, Int. J. Hydrogen Energy 39 (2014) 3810-3821.

[11] J. Huot, S. Amira, J. Lang, N. Skryabia, D. Fruchart, Improvement of hydrogen properties of magnesium alloys by cold rolling and forging, Mater. Sci. Eng. 63 (2014) 012-114.

[12] A. Revesz, M. Gajdics, E. Schafler, M. Calizzi, L. Pasquini, Dehydrogenation-hydrogenation characteristics of nanocrystalline $Mg_2Ni$ powders compacted by high-pressure torsion, J. Alloys Compds. 702 (2017) 84-91.

[13] S. Panda, J.J. Fundenberger, Y.J. Zhao, L. Toth, T. Grosdidier, Effect of initial powder type on the hydrogen storage properties of high-pressure torsion consolidated Mg, Int. J. Hydrogen Energy 42 (2017) 22438-22448.

[14] K. Edalati, M. Novelli, S. Itano, H. Li, E. Akiba, Z. Horita and T. Grosdidier, Effect of gradient-structure versus uniform nanostructure on hydrogen storage of Ti-V-Cr alloys: Investigation using ultrasonic SMAT and HPT processes, J. Alloys Compds. 737 (2018) 337-346.

[15] M. Novelli, K. Edalati, S. Itano, H. W. Li, E. Akiba, Z. Horita, T. Grosdidier, Microstructural details of hydrogen diffusion and storage in Ti–V–Cr alloys activated through surface and bulk severe plastic deformation, Int. J. Hydrogen Energy 45 (2020) 5326-5336.

[16] A.C. Asselli, D.R. Leiva, G.H. Cozentino, R. Floriano, J. Huot, T.T. Ishikawa, W.J. Botta, Hydrogen storage properties of $MgH_2$ processed by cold forging. J. Alloys Compds. 615 (2014) S719-S724.

[17] I. Popa, P. de Rango, D. Fruchart, S. Rivoirard, High-speed forged NdFe12-XVX compounds for bonded magnets, J. Mag. Materials 242-245 (2002) 1388-1390.

[18] P. de Rango, D. Fruchart, V. Aptukov, N. Skryabina, Fast forging: a new method to synthesize Mg-based alloys for hydrogen storage, Int. J. Hydrogen Energy 45 (2020) 7912-7916.

[19] F.G. Eisenberg, D.A. Zagnoli, J.J. Sheridan III, The effect of surface nickel on the hydriding-dehydriding kinetics of $MgH_2$, J. Less-Common Met. 74 (1980) 323-331.

[20] J.J. Reilly, R.H. Wiswall, Reaction of hydrogen with alloys of magnesium and nickel and the formation of $Mg_2NiH_4$, Inorg. Chem. 7 (1968) 2254-2256.

[21] J. Rodriguez-Carvajal, Recent Developments of the Program FULLPROF, Commission Powder Diffraction Newsletter 26 (2001) 12-19.

[22] B. Beausir and J.-J. Fundenberger, Analysis Tools for Electron and X-ray diffraction, ATEX - software, www.atex-software.eu, Université de Lorraine - Metz, 2017.

[23] T.T. Ueda, M. Tsukahara, Y. Kamiya, S. Kikuchi, Preparation and hydrogen storage properties of Mg-Ni-$Mg_2Ni$ laminate composites, J. Alloys Compds. 386 (2005) 253-257.

[24] N. Skryabina, V. Aptukov, P. de Rango, D. Fruchart, Effect of temperature on fast forging process of Mg-Ni samples for fast formation of $Mg_2Ni$ for hydrogen storage, Int. J. Hydrogen Energy 45 (2020) 3008-3015.

[25] H. Blomqvist and D. Noreus, Mechanically reversible conductor-insulator transition in $Mg_2NiH_4$, J. Appl. Phys. 91 (2002) 5141-5148.

[26] X.Q. Tran, S.D. McDonald, Q.F. Gu, T. Yamamoto, K. Shigematsu, K. Aso, E. Tanaka, S. Matsumura, K. Nogita, In-situ investigation of the hydrogen release mechanism in bulk $Mg_2NiH_4$, J. Power Sources 341 (2017) 130-138.

[27] T. Hongo, K. Edalati, M. Arita, J. Matsuda, E. Akiba, Z. Horit, Significance of grain boundaries and stacking faults on hydrogen storage properties of $Mg_2Ni$ intermetallics processed by high-pressure torsion, Acta Mater. 92 (2015) 46-54.

[28] Y.N. Wang, J.C. Huang, Texture analysis in hexagonal materials, Mater. Chem. Phys. 81 (2003) 11-26.

[29] S.V. Zherebtsov, G.S. Dyakonov, A.A. Salem, S.P. Malysheva, G.A. Salishchev, S.L. Semiatin, Evolution of grain and subgrain structure during cold rolling of commercial-purity titanium, Mater. Sci. Eng. A 528 (2011) 3474-3479.

[30] F.J. Humphreys, Quantitative metallography by electron backscattered diffraction, J. Microsc. 195 (1999) 170-185.

[31] J.K. Mason, C.A. Schuh, The generalized Mackenzie distribution: Disorientation angle distributions for arbitrary textures, Acta Mater. 57 (2009) 4186-4197.

[32] T. Al-Samman, G. Gottstein, Dynamic recrytallization during high temperature deformation of magnesium, Mater. Sci. Eng. A 490 (2008) 411-420.

[33] M.Y. Wang, R.L. Xin, B.S. Wang, Q. Liu, Effect of initial texture on dynamic recrystallization of AZ31 Mg alloy during hot rolling, Mater. Sci. Eng. A 528 (2011) 2941-2951.

[34] H.L. Kim, J.H. Lee, C.S. Lee, W. Bang, S.H. Ahn, Y.W. Chang, Shear band formation during hot compression of AZ31 Mg alloy sheets, Mater. Sci. Eng. A 558 (2012) 431-438.

[35] S. Sanyal, S. Kanodia, R. Saha, T.K. Bandyopadhyay, S. Mandal, Influence of hard plate hot forging temperature on the microstructure, texture and mechanical properties in a lean Mg-Zn-Al alloy, J. Alloys Compds. 800 (2019) 343-354.

[36] R.E.D. Mann, R.L. Hexemer Jr, I.W. Donaldson, D.P. Bishop, Hot deformation of an Al-Cu-Mg powder metallurgy alloy, Mater. Sci. Eng. A 528 (2011) 5476-5483.

[37] F. Wagner, N. Bozzolo, O. Van Landutyt, T. Grosdidier, Evolution of recrystallisation texture and microstructure in low alloyed titanium sheets, Acta Metall. 50 (2002) 1245-1259.

[38] A. Zaluska, L. Zaluski, J.O. Ström-Olsen, Synergy of hydrogen sorption in ball-milled hydrides of Mg and $Mg_2Ni$, J. Alloys Comp. 289 (1999) 197-206.

[39] B. Sakintuna, F. Lamari-Darkrim, M. Hirscher, Metal hydride materials for solid hydrogen storage: a review, Int. J. Hydrogen Energy 32 (2007) 1121-1140.

[40] V. Skrypniuk, E. Buchman, E. Rabkin, Y. Estrin, M. Popov, S. Jorgensen, The effect of equal channel angular pressing on hydrogen storage properties of a eutectic Mg-Ni alloy, J. Alloys Comp. 436 (2007) 99-106.

[41] M. Gajdics, M. Calizzi, L. Pasquini, E. Schafler, A. Revesz, Characterization of a nanocrystalline Mg-Ni alloy processed by high-pressure torsion during hydrogenation and dehydrogenation, Int. J. Hydrogen Energy 41 (2016) 9803-9809.

[42] K. Edalati, R. Uehiro, Y. Ikeda, H.W. Li, H. Emami, Y. Filinchuk, M. Arita, X. Sauvage, I. Tanaka, E. Akiba, Z. Horita, Design and synthesis of a magnesium alloy for room temperature hydrogen storage, Acta Mater. 149 (2018) 88-96.

[43] A. Revesz, M. Gajdics, L. Pasquini, G. Krallics, L. Peter, T. Spassov, Hydrogen storage of nanocrystalline Mg-Ni alloy processed by equal-channel angular pressing and cold rolling, Int. J. Hydrogen Energy 39 (2014) 9911-9917.

[44] R. Ölmez, G. Gakmak, T. Öztürk, Combinatorial search for hydrogen storage alloys: Mg-Ni and Mg-Ni-Ti, Int. J. Hydrogen Energy 35 (2010) 11957-11965.

[45] J.X. Zou, S. Long, X. Chen, X.Q. Zeng, W.J. Zeng, Preparation and hydrogen sorption properties of a Ni decorated Mg based Mg@Ni nano-composite, Int. J. Hydrogen Energy 40 (2015) 1820-1828.

[46] C.P Chen, B.H Liu, Z.P Li, J Wu, Q.D Wang, The activation mechanism of Mg-based hydrogen storage alloys, Phys. Chem. 181 (1993) 259-267.

[47] S. Orimo, H. Fuji, Materials science of Mg-Ni-based new hydrides, Appl. Phys. A 72 (2001) 167-186.

[48] X.J. Hou, R. Hu, T.B Zhang, H.C. Kou, J.S. Li, Hydrogenation thermodynamics of melt-spun magnesium rich Mg-Ni nanocrystalline alloys with the addition of multiwalled carbon nanotubes and $TiF_3$, J. Power Sources 306 (2016) 437-447.

[49] W.A. Johnson, R.F. Mehl, Reaction kinetics in processes of nucleation and growth, Trans. Metall. Soc. AIME 135 (1939) 396-415.

[50] W. Jander, Reaktionen im festen Zustande bei höheren Temperaturen. Reaktions-geschwindigkeiten endotherm verlaufender Umsetzungen, Z. Anorg. Allg. Chem. (in German) 163 (1927) 1-30.

[51] Y.P. Pang, Q. Li, A review on kinetic models and corresponding analysis methods for hydrogen storage materials, Int. J. Hydrogen Energy 41 (2016) 18072-18087.

[52] K.J. Zeng, T. Klassen, W. Oelerich, R. Bormann, Thermodynamic analysis of the hydriding process of Mg–Ni alloys, J. Alloys Compds. 283 (1999) 213-224.

[53] X.Q. Tran, S.D. McDonald, Q.F. Gu, K. Nogita, In-situ synchrotron X-ray diffraction investigation of the hydriding and dehydriding properties of a cast Mg-Ni alloy, J. Alloys Compds. 636 (2015) 249-256.